Geophysical Research Letters

RESEARCH LETTER
10.1029/2020GL089755

Key Points:

- Ocean Bottom Seismograph receiver functions constrain crustal structure near the extinct ridge of the South China Sea
- Thinned crust indicates reduced spreading rate and magma supply during the final stage of spreading
- Anomalously high *Vp*/*Vs* ratios are likely due to serpentine along faults formed in response to slowing spreading

Supporting Information:

- Supporting Information S1

Correspondence to:
T. Yang,
tyang@sustech.edu.cn

Citation:
Hung, T. D., Yang, T., Le, B. M., Yu, Y., Xue, M., Liu, B., et al. (2021). Crustal structure across the extinct mid-ocean ridge in South China Sea from OBS receiver functions: Insights into the spreading rate and magma supply prior to the ridge cessation. *Geophysical Research Letters*, *48*, e2020GL089755. https://doi.org/10.1029/2020GL089755

Received 31 JUL 2020
Accepted 18 DEC 2020

Crustal Structure Across the Extinct Mid-Ocean Ridge in South China Sea From OBS Receiver Functions: Insights Into the Spreading Rate and Magma Supply Prior to the Ridge Cessation

Tran Danh Hung[1,2], Ting Yang[1,3,4], Ba Manh Le[1], Youqiang Yu[5], Mei Xue[5], Baohua Liu[6], Chenguang Liu[6], Jian Wang[1], Mohan Pan[1], Phan Thien Huong[2], Fang Liu[4], and Jason P. Morgan[1]

[1]OBS Lab, Department of Ocean Science and Engineering, Southern University of Science and Technology, Shenzhen, China, [2]Department of Geophysics, Hanoi University of Mining and Geology, Hanoi, Vietnam, [3]Southern Marine Science and Engineering Guangdong Laboratory, Guangzhou, China, [4]Shanghai Sheshan National Geophysical Observatory, Shanghai, China, [5]State Key Laboratory of Marine Geology, Tongji University, Shanghai, China, [6]Key Laboratory of Marine Geology and Metallogeny, First Institute of Oceanography, MNR, Qingdao, China

Abstract The crust near an extinct mid-ocean ridge provides unique constraints on how its accretion and deformation responded to the cessation of spreading. Here we present crustal thickness and *Vp*/*Vs* measurements beneath 11 Ocean Bottom Seismograph sites that cross the South China Sea's extinct spreading axis. We find that the oceanic crust, which generally had only slight thickness changes once spreading started, abruptly thins at sites close to the extinct ridge axis. Abnormally high *Vp*/*Vs* ratios are obtained at several sites south of the ridge, indicating the presence of serpentine. These observations imply that, in its final stage, spreading changed to an ultraslow accretion style. As the axial crust thinned, normal faults and/or detachment faults began to form. Water could penetrate more deeply through these faults, and large fault slip could raise ultramafic peridotites to near or at the seafloor, creating favorable conditions for their enhanced serpentinization.

Plain Language Summary Mid-ocean ridges can both form and die. As a ridge dies, what happens to melt generation beneath the ridge axis? Clues exist in the oceanic crust near an extinct ridge that was created during the ridge's final stages of seafloor spreading. We explore a well-known extinct spreading center within the South China Sea. Using ocean bottom seismometers and the receiver function technique, we determine the thickness of the magmatic crust, and a parameter (*Vp*/*Vs*) that reflects the structure of the underlying crust. We find that, approaching the extinct spreading axis, the crust, typically uniform in thickness, thins significantly. This indicates that the melt supply decreases relative to spreading rate during the final stages of spreading. The *Vp*/*Vs* ratio at three sites nearest to the extinct spreading axis is abnormally high. Our inference is that the spreading rate and magma production has decreased to the point where large crustal faults can develop at several locations along the ridge. These faults provide pathways for seawater to reach and react with the uppermost mantle, forming minerals with higher *Vp*/*Vs* ratios which are then uplifted to the seafloor as the faults grow.

1. Introduction

The spreading rate along the global mid-ocean ridge (MOR) system varies greatly, from less than 1 to ~20 cm/yr (e.g., Dick et al., 2003). Many characteristics of oceanic crust exhibit substantial variations with MOR spreading rate. For example, although the thickness of most oceanic crust is relatively uniform, at slow to ultraslow MORs melt production is typically reduced due to conductive heat loss to the surface, which leads to the formation of thin magmatic crust (Bown & White, 1994; Chen, 1992) or even an "amagmatic" spreading segment without crust (Dick et al., 2003). On the other hand, spreading rate and crustal thickness are dominant factors in whether a ridge axis will develop a median valley with large detachment faults (e.g., Cannat et al., 2010; Escartín et al., 2008; Morgan & Chen, 1993). Therefore, oceanic crustal thickness and structure can serve as proxies that denote time-dependent changes in spreading rate and magma supply at a MOR.

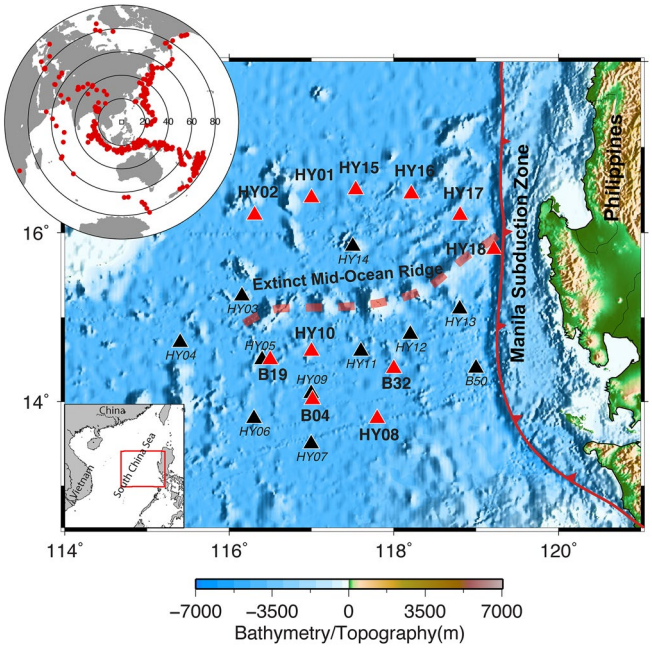

Figure 1. Map of the central subbasin of the South China Sea (SCS) showing the main geologic features in the region. Locations of working instruments in the OBS array are shown by red triangles. Locations of additional OBSs that were lost or failed to record good data are shown by black triangles. The heavy dashed line along the seamount chain depicts the location of the extinct spreading center axis (Briais et al., 1993; Li et al., 2014). The top inset shows the teleseismic events that we used, and the bottom inset shows the location of the regional map. OBS, Ocean Bottom Seismograph.

Extinct MORs represent an extreme case along the global MOR system, where spreading has stopped and the formation of the new oceanic crust has ceased. These features have been recognized in many places along the global spreading system (e.g., Batiza et al., 1982; Castillo et al., 2010; Davis et al., 2010; Delescluse et al., 2015; Fujioka et al., 1999; Livermore et al., 2000; Louden et al., 1996; Nishizawa & Oikawa, 2011). During the cessation of spreading along a propagating ridge where one spreading segment replaces another, it is seen that the "dying ridge" undergoes a transitional stage in which the spreading rate slows before the complete cessation of spreading. Similar behavior has been suggested to occur at other extinct spreading centers (e.g., Delescluse et al., 2015; Louden et al., 1996). However, these studies are few in number and have primarily looked at crustal thickness variations to infer magmatic variations without constraining other parameters, such as *Vp*/*Vs*, that can give additional insight into changing extents of brittle faulting and tectonism. Improved observations of this transitional stage will allow us to further explore how magma supply responds to slowing spreading, and how the mode of crustal accretion changes as a spreading center dies.

In the central subbasin of the South China Sea (SCS), there is a classic example of an extinct spreading axis. The SCS basin opened as a marginal sea at ~33 Ma and stopped spreading at ~15 Ma. Large amounts of postspreading volcanism continued for nearly 10 Myr (~13–3 Ma) to generate the Scarborough (also known as Huangyan-Zhenbei) seamount chain (e.g., Sibuet et al., 2016). Because of this postspreading volcanic activity, the spreading fabric along the extinct MOR axis has been masked by volcanoes and subsequent sediments. However, the timing of the onset and cessation of spreading has been confirmed by recent IODP drilling (Legs. 349) (e.g., Koppers, ; Li et al., 2015). Based on shipboard and deep-tow magnetic anomaly measurements, Briais et al.(1993) and Li et al.(2014) demonstrated that the spreading rate of the SCS gradually decreased with time during its lifetime, while strongly varying in the range of 20–80 mm/yr. Magnetic anomalies can estimate the average spreading rate between two adjacent distinguishable chrons, but in general, they cannot reveal a potential rate change within a relatively narrow time window. As a result, we lack detailed magnetic constraints on spreading rate during the death of the spreading axis in the SCS.

Here we use the data set collected by two passive-source Ocean Bottom Seismograph (OBS) array experiments in the central subbasin of the SCS near the extinct MOR (Figure 1). We employ the receiver function (RF) technique to determine the thickness and *Vp*/*Vs* ratio of crust near the extinct axis. The oceanic crustal thinning and change in crustal structure that we determine provide insights into the geodynamic and magmatic changes that occur when spreading wanes and stops.

2. Data and RF

Data used in this study were collected from passive-source OBS array experiments in the central subbasin of SCS, undertaken in 2012–2013 and 2014–2015 (Figure 1). In total, 36 OBSs were deployed near the extinct ridge and seamount chain. Seventeen stations were successfully recovered, with 11 recording valid data. Most of the recovered OBSs have data for 7–8 months, but three OBSs recorded only ~3 months of data due to various issues with the instrumentation (Le et al., 2018; Liu et al., 2014).

To determine the RF for each station, we apply the following data processing procedures to the OBS seismograms. We first determine the horizontal orientation of the OBS seismometer so that each event's radial and tangential components can be accurately obtained. This was achieved—to a typical accuracy of 8.0°—by analyzing long-period Rayleigh wave polarizations (Liu et al., 2014; Stachnik et al., 2012). Second, there

Table 1
OBS Information and RF Results, Including locations (Long, Lat), Water Depths (WDep), Horizontal orientations (HOri), Tilt Angles, Tilt directions (TDir), and Resultant Crustal Thickness H and Vp/Vs Measurements With Their Standard Deviations

Station	Long (°)	Lat (°)	WDep (m)	HOri (°)	Tilt (°)	TDir (°)	*H* (km)	*Vp/Vs* (*κ*)
B04	117.0110	14.0243	−4,246	185	6.5	280	7.0 ± 0.61	1.87 ± 0.13
B19	116.4990	14.5006	−4,301	350	6.5	110	6.7 ± 0.48	1.95 ± 0.10
B32	117.9990	14.3965	−3,859	110	0	–	7.3 ± 0.65	1.63 ± 0.12
HY01	117.0006	16.4054	−4,071	220	1.0	200	7.7 ± 1.18	1.88 ± 0.22
HY02	116.3061	16.2033	−3,750	20	3.5	160	7.8 ± 0.65	1.87 ± 0.20
HY08	117.7965	13.8004	−4,104	218	0.7	285	8.3 ± 0.39	1.94 ± 0.11
HY10	116.9983	14.5989	−4,276	166	0.8	215	5.2 ± 0.67	2.10 ± 0.11
HY15	117.537	16.5033	−3,753	154	16.3	5	7.5 ± 0.65	1.85 ± 0.11
HY16	118.2134	16.4513	−3,920	49	0.3	91	7.4 ± 0.46	1.79 ± 0.11
HY17	118.8037	16.2010	−3,870	330	2.0	131	6.1 ± 0.40	1.81 ± 0.08
HY18	119.2166	15.8003	−4,739	20	12.9	172	6.6 ± 0.62	1.73 ± 0.16

were pronounced clock errors in the data loggers of several OBSs (Le et al., 2018; Liu et al., 2014). Although the RF analysis is not sensitive to small clock drifts as long as they are synchronous for all three components, significant clock errors could lead to phase misidentifications in seismograms. Therefore, clock correction is still necessary. We use the time symmetry of Scholte waves in noise correction functions to correct clock timings (Le et al., 2018).

Additionally, we found that the seismometers in two OBSs had a significant tilt (Hung et al., 2019). Instrument tilt has a pronounced effect on RF analysis: the polarities of the *P* signature on RF in a back azimuth range can be flipped, and Moho-converted *Ps* phases can also be disturbed. A tilt noise analysis (Bell et al., 2015) can determine the tilting angle and direction, with which we can do a correction for instrument tilt. Apart from HY15 and HY18, the OBSs were found to have insignificant tilting angles (Table 1). Nonetheless, we correct for tilt in all three-component seismograms whenever the inferred tilt angle is larger than 2.5 degrees.

For the RF calculations, we consider only teleseismic events with magnitude greater than 5.0 and an epicentral distance from 20° to 95°. Seismograms are initially selected automatically based on their signal-to-noise ratios (SNR). For selected events, the SNRs of all three components must be greater than 4.0. We define the SNR as the ratio of the peak-to-peak amplitude of the predicted *P* arrival to the standard deviation of the time series in a 30-s window before the arrival. Automatically selected seismograms are then visually inspected to ensure that they are high-quality records. Representative examples of the three-component seismograms for all 11 OBSs are given in Figure S1. Each three-component seismogram is windowed from 30 s before to 80 s after the first *P* arrival predicted by the IASP91 Earth model. Records are then band-pass filtered with corner frequencies of 0.1 and 2.0 Hz.

To calculate the RFs, we use an iterative time-domain deconvolution (Ligorría & Ammon, 1999). This method uses a least squares minimization of the difference between the observed radial component seismogram and a predicted signal generated by convoluting an iteratively updated spike train with the vertical component. A water level of 0.001 and Gaussian width of 4.5 are adopted to stabilize the deconvolution. We obtained a total of 552 high-quality RFs (Figure 2, Figures S1 and S2). The number of usable events for each OBS varied from 17 to 90, depending on the length and quality of recording, with an average of about 50 good event records/station.

A loose sedimentary layer would induce a delayed first peak and strong reverberations in the resultant RFs (Yu et al., 2015). These are not observed in most of our RFs (Figure 2). This is likely due to the relatively thin sediment along this part of the SCS, as measured by an active-source study (Zhao et al., 2018) (Figure S3). A synthetic test indicates that (Figure S5), if the thickness of the seafloor sedimentary layer were less than 0.5 km, its influence on RF measurements would be small.

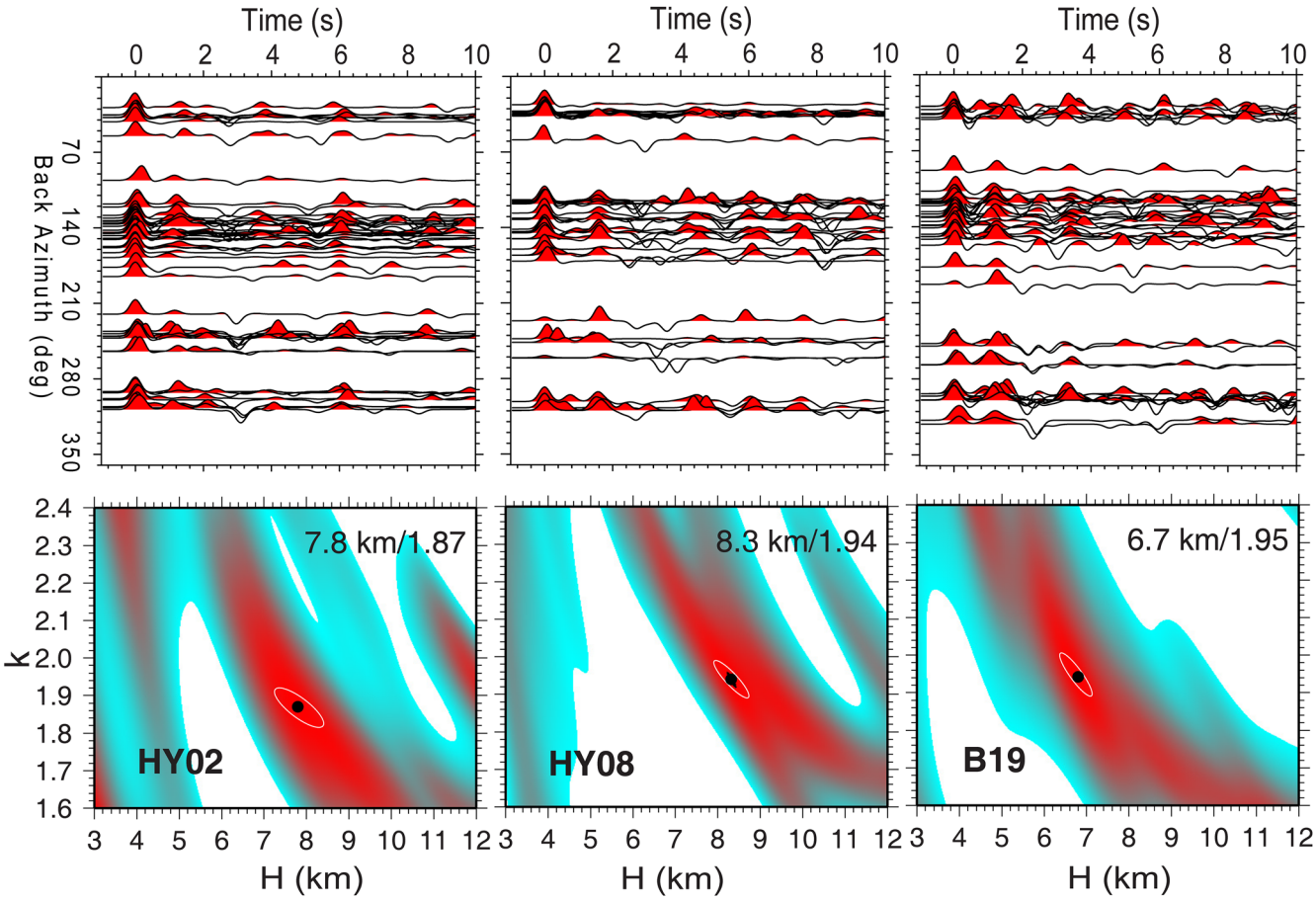

Figure 2. The RFs and *H-κ* stacking for OBS stations HY02, HY08, and B19. For each OBS, the upper panel shows the RFs from all events plotted against their back-azimuths, while the lower panel shows the H-κ stacking for the optimal crustal thickness and *Vp*/*Vs*. The RFs and *H-κ* stackings for other working OBSs are shown in Figure S2. OBS, Ocean Bottom Seismograph; RF, receiver function.

3. Crustal Thickness and *Vp*/*Vs*

From the 552 RFs calculated at all working OBS sites, we estimate the crustal thickness and vertically averaged *Vp*/*Vs* (*κ*) beneath each OBS using the *H-κ* stacking algorithm (Zhu & Kanamori, 2000). This algorithm involves stacking amplitudes along the predicted move-out curves for weighted Moho converted phases and multiples, including *PpPs*, *PsPs* + *PpSs* on each RF trace. The optimal thickness and *Vp*/*Vs* are obtained by maximizing the stacking amplitude of all RFs measured at each OBS. The weighting factors that we use for phases *Ps, PpPs, PsPs* + *PpSs* are 0.6, 0.3, 0.1, respectively.

The results of *H-κ* stacking at 11 OBS sites are shown in Figures 3 and 4, and Table 1. The measured crustal thickness ranges from 5.2 to 8.3 km. The average crustal thickness is 7.0 ± 0.6 km, slightly thicker than the "normal" range of oceanic crustal thickness (Bown & White, 1994; Chen, 1992; White et al., 2001). After excluding the average thickness of the sedimentary layer in this region (~0.5 km) (Zhao et al., 2018) (Figure S3), the actual oceanic thickness varies from 4.7 to 7.8 km. These lower values, 4.7 and 5.6 km at HY10 & HY17, are discernibly thinner than the expected thickness for normal oceanic crust. The measured spatial variation has a systematic pattern in that crustal thicknesses at sites near the extinct ridge are thin, while crustal thicknesses increase away from the extinct axis (Figures 3 and 4).

Vp/*Vs* results are shown in Figure 3 and Table 1. Measured ratios fall into the range of 1.63–2.10, with an average of 1.86. These values are slightly higher than anticipated for a mafic oceanic crust composition (Christensen, 1996; Holbrook et al., 1992; Zandt & Ammon, 1995). The spatial distribution of *Vp*/*Vs* ratios appears to show a strikingly asymmetric pattern: while the ratios at the northern sites are less than 1.9 (see

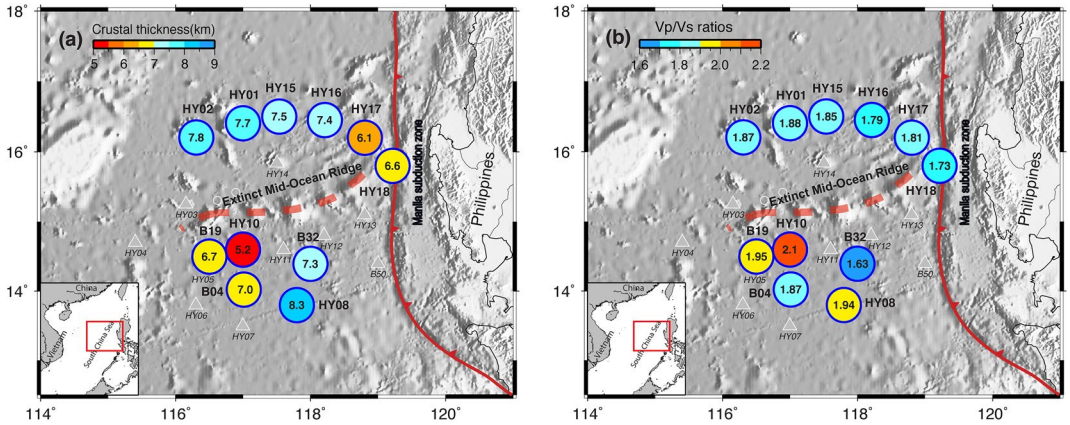

Figure 3. Mapview of crustal thickness and *Vp*/*Vs* beneath the 11 measured OBS sites in the central subbasin of the SCS. The number inside each circle and its color reflect its inferred crustal thickness (crust + sediments) in km (a) & its *Vp*/*Vs* value (b). OBS, Ocean Bottom Seismograph; SCS, South China Sea.

Figure 3b), those to the south generally have larger values. Three southern sites HY08, B19, and HY10, all have ratios close to or exceeding 2.0.

Note that the absolute values of crustal thickness and *Vp/Vs* are sensitive to the average crustal *P*-wave velocity $\left(\overline{Vp}\right)$ that is assumed in the stacking. Previous studies indicate the $\overline{Vp}$ of the oceanic crust is around 6.0 km/s (e.g., Hyndman, 1979). However, this value can vary strongly depending on the age, sediment cover, and internal layering of the oceanic crust. We calculated $\overline{Vp}$ based on active source seismic profiles near the extinct ridge (Zhao et al., 2018). The value is 5.1 km/s (See Supporting Information for further details). However, these profiles were carried out on or very close to an axis that experienced extreme postspreading volcanism until 3 Ma. Therefore, the temperature of the crust may be anomalously high. Our OBS sites are sited on older oceanic crust; their $\overline{Vp}$ should be higher. Therefore, we extrapolate from a value of 5.5 km/s. To see how sensitive the results are to the assumed $\overline{Vp}$, we test different values of $\overline{Vp}$ (5.1 and 5.8 km/s) and find that, although the absolute thickness changes notably beneath each OBS, the varying pattern of crustal thickness versus distance persists (Figure S4). *Vp*/*Vs* ratios only change negligibly (<2%) for different assumed values of $\overline{Vp}$.

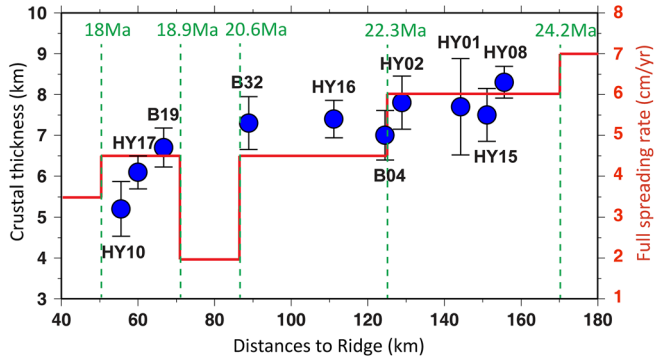

Figure 4. Crustal thicknesses (crust + sediments) beneath 10 OBS sites plotted against the distance to the extinct ridge axis in the central subbasin of the SCS. The short vertical line at each blue circle gives the standard deviation of the thickness measurement at each OBS site. The full spreading rate determined from magnetic anomaly measurements (Li et al., 2014) is also shown (red line and y-axis to the right) for comparison. Corresponding seafloor ages estimated from Li et al. (2014) (green numbers) are noted above transitions in magnetic-anomaly inferred spreading rates. We note that the OBS HY18 is located right on the MOR, where the crust was thickened by postspreading volcanism (Sibuet et al., 2016). Thus, this measurement is not included in this plot. MOR, mid-ocean ridge; OBS, Ocean Bottom Seismograph; SCS, South China Sea.

4. Discussion

4.1. Insights Into the Time Variation of Spreading Rate and Magma Emplacement Prior to the Cessation of Spreading at a Ridge Axis

As shown in Figure 4, the thicknesses of OBS sites whose distances to the ridge are greater than 60 km are in the normal range of oceanic crust (White et al., 2001). Crustal thicknesses (crust + sediments) appear to linearly increase from ~6.5 km 60-km from the extinct axis to ~8.5 km 160-km from the axis. The two sites closer than 60 km from the ridge have crust that is significantly thinner than normal, and whose thickness decreases toward the extinct ridge axis. An overall decreasing pattern of the spreading rate is also inferred from magnetic anomaly modeling (Li et al., 2014), with an average full spreading rate of ~6.5 cm/yr at distances >90 km from the axis, and an average rate of ~3.5 cm/yr at distances <90 km from the axis. The slower spreading region broadly correlates with the region of reduced crustal thickness within ~75 km from the axis (Figure 4).

The varying pattern of crustal thickness versus distance to the ridge has important implications for the change of the spreading rate of MOR in the SCS. Both global observations (e.g., Dick et al., 2003; White et al., 1992, 2001) and numerical models (e.g., Reid & Jackson, 1981) indicate that seismic crustal thickness should show little dependence on spreading rate, unless the temperature of the underlying mantle source changes (Note that Zhou et al., 2020 suggest that satellite altimetry-based gravity observations imply a change to slightly thinner crust at fast and ultra-fast spreading rates, but this inference has yet to be confirmed by seismic observations). Only at those ridges whose full spreading rate is less than 2.0 cm/yr would crustal thickness be predicted to decrease, in response to the amount of melting being reduced by deepening of the top boundary of the melting region due to vertical conductive heat loss beneath a very slow-spreading ridge (e.g., Bown & White, 1994; Chen, 1992; Reid & Jackson, 1981).

When spreading in the SCS-approached cessation, the spreading rate decreased significantly (Figure 4). Site HY10, closest to the ridge, has the thinnest crust (~4.7 km exclusive of 0.5 km thick sediments). Thinning crust appears to correlate with a significant decrease in spreading rate, although the inferred spreading rate (~2–4 cm/yr, see Figure 4) appears to be slightly above the ~2 cm/yr that Dick et al. (2003) proposed for where the transition to the ultraslow spreading regime takes place. However, the rapid reduction in crustal thickness at ~60 km from the extinct axis is superimposed on the overall secular decrease in crustal thickness shown in Figure 4. We propose that this secular decrease reflects overall cooling of the asthenosphere beneath the SCS with time, which led to a ~2 km decrease in crustal thickness prior to the change to ultraslow-like rates of crustal production. The slowdown likely happened at the magnetic anomaly inferred sea floor age of ~18.5 Ma at the site of OBS 17 where anomalous thinning is first observed (Figure 4).

4.2. Insights Into the Crustal and Uppermost Mantle Composition

Vp/*Vs* ratios provide another useful constraint on the evolution of oceanic crustal structure. While the values of *Vp*/*Vs* at sites in the north of the extinct MOR are comparable to the average of regular oceanic crust composition (Bratt & Solomon, 1984; Christensen, 1996, 2004), southern sites have significantly higher *Vp*/*Vs*. In particular, the ratios at these three sites are close to or even greater than 2.0. These anomalously high *Vp*/*Vs* ratios hint that there could be a large fraction of serpentine in the crust beneath those sites (Christensen, 2004), as serpentinite is the only major oceanic rock-type with such high *Vp*/*Vs* ratios. Serpentinites have been widely observed and sampled at slow and ultraslow spreading ridges (Cannat et al., 1997; Dick et al., 2003; Gràcia et al., 2000; Guillot et al., 2015; Kelemen et al., 2004; Michael et al., 2003; Sauter et al., 2013). Large offset normal faults and detachment faults commonly form in the oceanic crust constructed at such ridges. These crustal-scale faults can act as channels by which water can reach and react with underlying mantle, while also acting as a conveyor belt that brings up mantle peridotites to the depths of hydrothermal circulation and serpentinization (Cannat et al., 2010). Serpentinization leads to a decrease in density and seismic velocities, and a significant increase in *Vp*/*Vs* (Carlson & Miller, 1997; Minshull et al., 1998). Depending on the volume percent of serpentine, *Vp*/*Vs* can reach as high as 2.2 for oceanic mantle rocks (Christensen, 2004; Hyndman & Peacock, 2003).

We conjecture that, when the spreading rate slowed to near the slow/ultraslow range at the ridge axis in the central subbasin of the SCS and the magma supply had also significantly diminished, then large offset normal faults and detachment faults could easily develop in the median valley-type ridge axis (Morgan & Chen, 1993). This new axial structure with its large-offset normal faults was an environment where serpentinite would form near fault escarpments (Cannat et al., 2010). Sites HY10, HY08, and B19 were locations where this type of partially serpentinized crust would develop at the axis. Note that since serpentine is typically associated with wavespeeds that mimic oceanic crust (except in terms of its higher *Vp*/*Vs* ratio), magmatic crustal thicknesses could even be thinner than we determined for these sites. In this case, the inferred cooling of the ridge's mantle source would be even larger at the time when spreading ceased.

On the other hand, the asymmetric pattern of *Vp*/*Vs* ratios with respect to the fossil axis may reflect the different thermal state of mantle north and south of the ridge (e.g., Zhang et al., 2020). In the north, many tomographic studies have found large low-wavespeed bodies in the upper mantle below the region of Hainan island and its neighboring margin, anomalies that have been interpreted to be the seismic expression of a Hainan Plume (e.g., Huang et al., 2006; Lei et al., 2009; Xia et al., 2018). Xu et al. (2012) even proposed that the ridge was fed through a sublithospheric asthenospheric channel originating from Hainan Island.

Therefore, the upper mantle in the northern side of the basin appears to have had higher temperatures. Shallower Curie depths in the north (e.g., Li et al., 2010) and the fact that strong postspreading volcanism only occurred in the northern subbasin also hint at a higher local sublithospheric temperature in this region. This higher temperature, especially if associated with the intrusion of magmas into overlying crust, could impede the development of brittle crustal faults, and so limit the extent of serpentinization.

Curiously, some volcanism persisted after the cessation of spreading. We see direct evidence for this at site HY18 on the extinct axis, where the crustal thickness is inferred to be ~6.6 km. This implies the later addition of several kilometer of seamount volcanism, with other continued volcanism building the later-to-form Scarborough seamount chain.

5. Conclusions

Crustal thicknesses and *Vp*/*Vs* in the central subbasin of the SCS are determined by performing RF analyses based on data collected in two passive-source OBS experiments. While most OBS sites indicate oceanic crust of normal thickness, the crust near the extinct ridge appears to be noticably thinner. We attribute the pattern of crustal thickness versus distance to the ridge to arise from two factors: (1) an overall secular decline in the temperature of the astheneosphere beneath the SCS spreading center, and (2) a reduction in spreading rate to near ultraslow rates as the ridge approached its cessation. These two influences led to decreased magma supply, thinner crust, and a change from axial high to median-valley-type axial structure at the time when spreading ultimately ceased.

The *Vp*/*Vs* in our OBS sites indicates a mafic oceanic crustal composition. However, three OBS sites show anomalously high *Vp*/*Vs* ratios. These high values are difficult to explain except by the presence of a significant volume fraction (40% as a minimum) of serpentinized peridotite, which implies that a fraction of the uppermost mantle experienced serpentinization and was incorporated into the oceanic crust. This is a further indication that large offset normal faults and detachment faults developed at the ridge axis during the final phase of spreading along the failing rift.

Data Availability Statement

The seismograms used to generate the RFs can be accessed at http://doi.org/10.5281/zenodo.3968504.

Acknowledgments
This study was supported by the National Natural Science Foundation of China (92058209, 41676033, 41606043, and 91128209) and Shenzhen SciTech Commission (KQTD20170810111725321, JCYJ20180504170422082; GJHZ20170313101107497). We thank two anonymous reviewers for their constructive comments.

References

Batiza, R., Oestrike, R., & Futa, K. (1982). Chemical and isotopic diversity in basalts dredged from the East Pacific Rise at 10°S, the fossil Galapagos Rise and the Nazca plate. *Marine Geology*, *49*, 115–132. https://doi.org/10.1016/0025-3227(82)90032-9

Bell, S. W., Forsyth, D. W., & Ruan, Y. (2015). Removing noise from the vertical component records of ocean-bottom seismometers: Results from year one of the cascadia initiative. *Bulletin of the Seismological Society of America*, *105*(1), 300–313. https://doi.org/10.1785/0120140054

Bown, J. W., & White, R. S. (1994). Variation with spreading rate of oceanic crustal thickness and geochemistry. *Earth and Planetary Science Letters*, *121*(3–4), 435–449. https://doi.org/10.1016/0012-821X(94)90082-5

Bratt, S., & Solomon, S. (1984). Compressional and shear wave structure of the East Pacific Rise at 11°20' N: Constraints from three-component ocean bottom seismometer data. *Journal of Geophysical Research*, *89*(B7), 6095–6110.

Briais, A., Patriat, P., & Tapponnier, P. (1993). Updated interpretation of magnetic anomalies and seafloor spreading stages in the south China Sea: Implications for the Tertiary tectonics of Southeast Asia. *Journal of Geophysical Research*, *98*(B4), 6299–6328. https://doi.org/10.1029/92JB02280

Cannat, M., Fontaine, F., & Escartín, J. (2010). Serpentinization and associated hydrogen and methane fluxes at slow spreading ridges. In P. A. Rona, C. W. Devey, J. Dyment et al. (Eds.), *Diversity of hydrothermal systems on slow spreading ocean ridges* (pp. 241–264). Washington, DC: American Geophysical Union.

Cannat, M., Lagabrielle, Y., Bougault, H., Casey, J., De Coutures, N., Dmitriev, L., & Fouquet, Y. (1997). Ultramafic and gabbroic exposures at the Mid-Atlantic Ridge: Geological mapping in the 15 N region. *Tectonophysics*, *279*(1-4), 193–213.

Carlson, R. L., & Miller, D. J. (1997). A new assessment of the abundance of serpentinite in the oceanic crust. *Geophysical Research Letters*, *24*(4), 457–460.

Castillo, P. R., Clague, D. A., Davis, A. S., & Lonsdale, P. F. (2010). Petrogenesis of Davidson Seamount lavas and its implications for fossil spreading center and intraplate magmatism in the eastern Pacific. *Geochemistry, Geophysics, Geosystems*, *11*, Q02005. https://doi.org/10.1029/2009GC002992

Chen, Y. J. (1992). Oceanic crustal thickness versus spreading rate. *Geophysical Research Letters*, *19*(8), 753–756.

Christensen, N. I. (1996). Poisson's ratio and crustal seismology. *Journal of Geophysical Research*, *101*(B2), 3139–3156. https://doi.org/10.1029/95JB03446

Christensen, N. I. (2004). Serpentinites, peridotites, and seismology. *International Geology Review*, *46*(9), 795–816. https://doi.org/10.2747/0020-6814.46.9.795

Davis, A. S., Clague, D. A., Paduan, J. B., Cousens, B. L., & Huard, J. (2010). Origin of volcanic seamounts at the continental margin of California related to changes in plate margins. *Geochemistry, Geophysics, Geosystems*, *11*, Q05006. https://doi.org/10.1029/2010GC003064

Delescluse, M., Funck, T., Dehler, S. A., Louden, K. E., & Watremez, L. (2015). The oceanic crustal structure at the extinct, slow to ultraslow Labrador Sea spreading center. *Journal of Geophysical Research: Solid Earth*, *120*(7), 5249–5272. https://doi.org/10.1002/2014JB011739

Dick, H. J. B., Lin, J., & Schouten, H. (2003). An ultraslow-spreading class of ocean ridge. *Nature*, *426*(6965), 405–412. https://doi.org/10.1038/nature02128

Escartín, J., Smith, D. K., Cann, J., Schouten, H., Langmuir, C. H., & Escrig, S. (2008). Central role of detachment faults in accretion of slow-spreading oceanic lithosphere. *Nature*, *455*(7214), 790–794.

Fujioka, K., Okino, K., Kanamatsu, T., Ohara, Y., Ishizuka, O., Haraguchi, S., & Ishii, T. (1999). Enigmatic extinct spreading center in the West Philippine backarc basin unveiled. *Geology*, *27*(12), 1135–1138.

Gràcia, E., Charlou, J. L., Radford-Knoery, J., & Parson, L. M. (2000). Non-transform offsets along the Mid-Atlantic Ridge south of the Azores (38 N–34 N): ultramafic exposures and hosting of hydrothermal vents. *Earth and Planetary Science Letters*, *177*(1–2), 89–103.

Guillot, S., Schwartz, S., Reynard, B., Agard, P., & Prigent, C. (2015). Tectonic significance of serpentinites. *Tectonophysics*, *646*, 1–19. https://doi.org/10.1016/j.tecto.2015.01.020

Holbrook, W. S., Mooney, W. D., & Christensen, N. I. (1992). The seismic velocity structure of the deep continental crust in Continental Lower Crust. *Developments in Geotectonics*, *23*(1987), 1–34.

Huang, J., & Zhao, D. (2006). High-resolution mantle tomography of China and surrounding regions. *Journal of Geophysical Research*, *111*, B09305. https://doi.org/10.1029/2005JB004066

Hung, T. D., Yang, T., Le, B. M., & Yu, Y. (2019). Effects of failure of the ocean-bottom seismograph leveling system on receiver function analysis. *Seismological Research Letters*, *90*(3), 1191–1199. https://doi.org/10.1785/0220180276

Hyndman, R. D. (1979). Poisson's ratio in the oceanic crust–a review. *Developments in Geotectonics*, *15*, 321–333.

Hyndman, R. D., & Peacock, S. M. (2003). Serpentinization of the forearc mantle. *Earth and Planetary Science Letters*, *212*, 417–432. https://doi.org/10.1016/S0012-821X(03)00263-2

Kelemen, P. B., Kikawa, E., & Miller, D. J., & Shipboard Scientific Party of ODP Leg 209. (2004). Proceedings of the ocean drilling program initial reports (Vol. 209). College Station, TX: Ocean Drilling Program.

Le, B. M., Yang, T., Chen, Y. J., & Yao, H. (2018). Correction of OBS clock errors using Scholte waves retrieved from cross-correlating hydrophone recordings. *Geophysical Journal International*, *212*(2), 891–899. https://doi.org/10.1093/gji/ggx449

Lei, J., Zhao, D., Steinberger, B., Wu, B., Shen, F., & Li, Z. (2009). New seismic constraints on the upper mantle structure of the Hainan plume. *Physics of the Earth and Planetary Interiors*, *173*(1-2), 33–50.

Li, C. F., Li, J., Ding, W., Franke, D., Yao, Y., Shi, H., et al. (2015). Seismic stratigraphy of the central South China Sea basin and implications for neotectonics. *Journal of Geophysical Research: Solid Earth*, *120*(3), 1377–1399. https://doi.org/10.1002/2014JB011686

Li, C. F., Shi, X., Zhou, Z., Li, J., Geng, J., & Chen, B. (2010). Depths to the magnetic layer bottom in the South China Sea area and their tectonic implications. *Geophysical Journal International*, *182*(3), 1229–1247.

Li, C., Xu, X., Lin, J., Sun, Z., Peleo-Alampay, A., & Tejada, M. (2014). Ages and magnetic structures of the South China Sea constrained by deep tow magnetic surveys and IODP Expedition 349. *Geochemistry, Geophysics, Geosystems*, *15*(12), 4958–4983. https://doi.org/10.1002/2014GC005567

Ligorría, J. P., & Ammon, C. J. (1999). Iterative deconvolution and receiver function estimation. *Bulletin of the Seismological Society of America*, *89*, 1395–1400.Retrieved from http://www.bssaonline.org/content/89/5/1395.abstract

Liu, C., Hua, Q., Pei, Y., Yang, T., Xia, S., Xue, M., et al. (2014). Passive-source ocean bottom seismograph (OBS) array experiment in South China Sea and data quality analyses. *Chinese Science Bulletin*, *59*(33), 4524–4535. https://doi.org/10.1007/s11434-014-0369-4

Livermore, R., Balanyá, J. C., Maldonado, A., Martínez, J. M., Rodríguez-Fernández, J., de Galdeano, C. S., et al. (2000). Autopsy on a dead spreading center: The Phoenix Ridge, Drake Passage, Antarctica. *Geology*, *28*(7), 607–610.

Louden, K. E., Osler, J. C., Srivastava, S. P., & Keen, C. E. (1996). Formation of oceanic crust at slow spreading rates: New constraints from an extinct spreading center in the Labrador Sea. *Geology*, *24*(9), 771–774.

Michael, P. J., Langmuir, C. H., Dick, H. J. B., Snow, J. E., Goldstein, S. L., Graham, D. W., et al. (2003). Magmatic and amagmatic seafloor generation at the ultraslow-spreading Gakkel ridge, Arctic Ocean. *Nature*, *423*(6943), 956–961.

Minshull, T. A., Muller, M. R., Robinson, C. J., White, R. S., & Bickle, M. J. (1998). Is the oceanic Moho a serpentinization front? In R. A. Mills, & K. Harrison (Eds.), Modern ocean floor processes and the geological record (Vol. 148, pp. 71–80). London, UK: Geological Society of London.

Morgan, J. P., & Chen, Y. J. (1993). Dependence of ridge-axis morphology on magma supply and spreading rate. *Nature*, *364*(6439), 706–708.

Nishizawa, A., Kaneda, K., & Oikawa, M. (2011). Backarc basin oceanic crust and uppermost mantle seismic velocity structure of the Shikoku Basin, south of Japan. *Earth, Planets and Space*, *63*(2), 151–155.

Reid, I., & Jackson, H. R. (1981). Oceanic spreading rate and crustal thickness. *Marine Geophysical Researches*, *5*(2), 165–172. https://doi.org/10.1007/BF00163477

Sauter, D., Cannat, M., Rouméjon, S., Andreani, M., Birot, D., Bronner, A., et al. (2013). Continuous exhumation of mantle-derived rocks at the Southwest Indian Ridge for 11 million years. *Nature Geoscience*, *6*(4), 314–320.

Sibuet, J. C., Yeh, Y. C., & Lee, C. S. (2016). Geodynamics of the South China Sea. *Tectonophysics*, *692*, 98–119. https://doi.org/10.1016/j.tecto.2016.02.022

Stachnik, J. C., Sheehan, A. F., Zietlow, D. W., Yang, Z., Collins, J., & Ferris, A. (2012). Determination of New Zealand Ocean Bottom Seismometer Orientation via Rayleigh-Wave Polarization. *Seismological Research Letters*, *83*(4), 704–713. https://doi.org/10.1785/0220110128

White, R. S., McKenzie, D., & O'Nions, R. K. (1992). Oceanic crustal thickness from seismic measurements and rare earth element inversions. *Journal of Geophysical Research*, *97*(B13), 19683. https://doi.org/10.1029/92JB01749

White, R. S., Minshull, T. A., Bickle, M. J., & Robinson, C. J. (2001). Melt generation at very slow-spreading oceanic ridges: Constraints from geochemical and geophysical data. *Journal of Petrology*, *42*(6), 1171–1196. https://doi.org/10.1093/petrology/42.6.1171

Xia, S., Zhao, F., Zhao, D., Fan, C., Wu, S., Mi, L., et al. (2018). Crustal plumbing system of post-rift magmatism in the northern margin of South China Sea: New insights from integrated seismology. *Tectonophysics*, *744*, 227–238.

Xu, Y., Wei, J., Qiu, H., Zhang, H., & Huang, X. (2012). Opening and evolution of the South China Sea constrained by studies on volcanic rocks: Prelimimary results and a research design. *Chinese Science Bulletin*, *57*, 3150–3164. https://doi.org/10.1007/s11434-011-4921-1

Yu, Y., Song, J., Liu, K. H., & Gao, S. S. (2015). Determining crustal structure beneath seismic stations overlying a low-velocity sedimentary layer using receiver functions. *Journal of Geophysical Research: Solid Earth*, *120*(5), 3208–3218. https://doi.org/10.1002/2014JB011610

Zandt, G., & Ammon, C. J. (1995). Continental crust composition constrained by measurements of crustal Poisson's ratio. *Nature*, *374*(6518), 152–154.

Zhang, F., Lin, J., Zhang, X., Ding, W., Wang, T., & Zhu, J. (2020). Asymmetry in oceanic crustal structure of the South China Sea basin and its implications on mantle geodynamics. *International Geology Review*, *62*(7-8), 840–858.

Zhao, M., He, E., Sibuet, J.-C., Sun, L., Qiu, X., Tan, P., et al. (2018). Post seafloor spreading volcanism in the central east South China Sea and its formation through an extremely thin oceanic crust. *Geochemistry, Geophysics, Geosystems*, *19*. https://doi.org/10.1002/2017GC007034

Zhou, D., Li, C. F., Zlotnik, S., & Wang, J. (2020). Correlations between oceanic crustal thickness, melt volume, and spreading rate from global gravity observation. *Marine Geophysical Research*, *41*(3), 1–16.

Zhu, L., & Kanamori, H. (2000). Moho depth variation in southern California from teleseismic receiver functions. *Journal of Geophysical Research*, *105*(B2), 2969–2980.